© 2020. Published by The Company of Biologists Ltd | Journal of Cell Science (2020) 133, jcs237503. doi:10.1242/jcs.237503

RESEARCH ARTICLE

# Mechanisms of malignancy in glioblastoma cells are linked to mitochondrial $Ca^{2+}$ uniporter upregulation and higher intracellular $Ca^{2+}$ levels

**Xiaoyun Li[1], Renza Spelat[1], Anna Bartolini[2], Daniela Cesselli[2,3], Tamara Ius[4], Miran Skrap[4], Federica Caponnetto[3], Ivana Manini[3], Yili Yang[5] and Vincent Torre[1,5,*]**

## ABSTRACT

Glioblastoma (GBM) is one of the most malignant brain tumours and, despite advances in treatment modalities, it remains largely incurable. $Ca^{2+}$ regulation and dynamics play crucial roles in different aspects of cancer, but they have never been investigated in detail in GBM. Here, we report that spontaneous $Ca^{2+}$ waves in GBM cells cause unusual intracellular $Ca^{2+}$ ($[Ca^{2+}]_i$) elevations (>1 µM), often propagating through tumour microtubes (TMs) connecting adjacent cells. This unusual $[Ca^{2+}]_i$ elevation is not associated with the induction of cell death and is concomitant with overexpression of mitochondrial $Ca^{2+}$ uniporter (MCU). We show that *MCU* silencing decreases proliferation and alters $[Ca^{2+}]_i$ dynamics in U87 GBM cells, while *MCU* overexpression increases $[Ca^{2+}]_i$ elevation in human astrocytes (HAs). These results suggest that changes in the expression level of MCU, a protein involved in intracellular $Ca^{2+}$ regulation, influences GBM cell proliferation, contributing to GBM malignancy.

This article has an associated First Person interview with the first author of the paper.

**KEY WORDS: MCU, $Ca^{2+}$ waves, Glioblastoma, Malignancy**

## INTRODUCTION

When primary glioblastoma (GBM; World Health Organization grade IV glioma) cells derived from patients are implanted in mouse brains, long and thin membrane protrusions originating from the cell body of the GBM cells are observed (Osswald et al., 2015). These thin protrusions, which can be as long as hundreds of microns and connect tumour cells in a multicellular network, are referred to as tumour microtubes (TMs). TMs have two features possibly contributing to GBM malignancy: they provide a way for GBM to invade and infiltrate, and they form one large syncytium that confers to the cellular network resistance to radiotherapy (Osswald et al., 2015; Osuka and Van Meir, 2017). Oncotherapy, based on either radiotherapy or chemotherapy, is usually associated with increased intracellular $Ca^{2+}$ ($[Ca^{2+}]_i$) (McFerrin et al., 2012; Tombal et al., 2002), and the control of $[Ca^{2+}]_i$ plays major roles in healthy and cancerous cells. Indeed, when $[Ca^{2+}]_i$ is elevated to micromolar levels, cells usually undergo apoptosis within 6 h (Tombal et al., 2002). The unusual resistance of GBM cells to oncotherapy has been attributed to the ability of TMs to facilitate $Ca^{2+}$ fluxes among different GBM cells, leading to the distribution of $[Ca^{2+}]_i$ away from damaged cells to all the other cells connected to it by the TMs. However, it is possible that GBM cells also have an intrinsic resistance – originating from their altered genomic landscape – to the elevation of $[Ca^{2+}]_i$, as we argue in the present paper.

Mitochondria accumulate large amounts of $Ca^{2+}$ and contribute to the maintenance of a low resting $[Ca^{2+}]_i$ (Foskett and Philipson, 2015): if $[Ca^{2+}]_i$ exceeds a threshold in the micromolar range, cells trigger metabolic pathways leading to cell death (Liu et al., 2015). $Ca^{2+}$ influx into mitochondria is mediated by mitochondrial $Ca^{2+}$ uniporter (MCU), and genetic ablation of *Mcu* decreases mitochondrial $Ca^{2+}$ uptake (Hamilton et al., 2018), while persistent MCU activity enhances mitochondrial $Ca^{2+}$ uptake (Dong et al., 2017). It has been proposed that cancer stem cells share several properties of adult neural stem cells, in particular altered $Ca^{2+}$ regulation (Leclerc et al., 2016). On the basis of a bioinformatics analysis, several genes involved in $Ca^{2+}$ regulation with altered expression in GBM cells have been identified, among which *MCU* has been found to be overexpressed (Robil et al., 2015). There is now considerable evidence suggesting crucial roles for MCU and its regulators in cancer (Mammucari et al., 2017), but the exact function of MCU in GBM cells has not yet been fully described or understood.

To perform measurements of $Ca^{2+}$ dynamics and $[Ca^{2+}]_i$, we looked for U87 GBM cells connected by TMs in a single layer (Fig. 1A), in which $Ca^{2+}$ measurements are feasible and reliable. We also observed TMs in cultures of the U251, T98G GBM cell lines and in glioblastoma stem cells (GSCs) from patients cultured in adhesion. We analysed $Ca^{2+}$ transients in the somas and TMs of U87 cells using the fluorescent $Ca^{2+}$ probe Fluo-4 AM and with ratiometric $Ca^{2+}$ imaging using Fluo-4 AM and Fura Red AM, providing a quantitative measure of $Ca^{2+}$ transients (Assinger et al., 2015). Our results show some unusual properties of $Ca^{2+}$ dynamics in GBM cells: first, spontaneously occurring transients originating in the middle of TMs did not always propagate to the somas of connected cells, but large $Ca^{2+}$ waves originating in the somas propagated along the TMs more easily; second, spontaneous $Ca^{2+}$ transients in U87 cells and GSCs from patients could reach values up to 1–3 µM for long durations and not lead to cell death; and third, MCU, a protein involved in the influx of $Ca^{2+}$ into the mitochondria, is overexpressed in GBM cells.

Our results suggest that the mitochondrial $[Ca^{2+}]$ overload after overexpression of *MCU*, causes large and unusual $[Ca^{2+}]_i$

[1]Neurobiology Sector, International School for Advanced Studies (SISSA), 34136 Trieste, Italy. [2]Institute of Pathology, University Hospital of Udine, 33100 Udine, Italy. [3]Department of Medicine, University of Udine, 33100 Udine, Italy. [4]Neurosurgery Unit, Department of Neurosciences, University Hospital of Udine, 33100 Udine, Italy. [5]Joint SISSA-ISM Laboratory, Suzhou Institute of Systems Medicine, Chinese Academy of Medical Sciences, 215000 Suzhou, Jiangsu, China.

*Author for correspondence (torre@sissa.it)

T.I., 0000-0003-3741-0639; I.M., 0000-0002-3319-7749; V.T., 0000-0001-8133-3584

**Received 6 August 2019; Accepted 28 January 2020**

Journal of Cell Science (2020) 133, jcs237503. doi:10.1242/jcs.237503

dynamics. Moreover, a higher MCU level in GBM cells promotes cell proliferation, which is an important factor contributing to GBM malignancy, possibly through activation of the $Ca^{2+}$-calmodulin complex and calmodulin-dependent protein kinase II (CaMKII) (Fischer et al., 2013), and specific transcription factors, such as members of the cAMP response element-binding protein (CREB) family (Shanmughapriya et al., 2015).

## RESULTS

### TMs connecting separated GBM cells

The proliferation and migration of cultured GBM cells were followed by live-cell imaging, in which an image was acquired every 1 or 2 min for several days. When GBM cells were imaged under bright-field illumination, thin structures connecting two GBM cells reminiscent of tumour TMs were detected (Fig. 2A). When GBM cells were either stained with the fluorescent membrane marker Vybrant™ DiD or labelled with the fluorescent probe mCherry, TMs were better visualized, and their dynamics could be followed for several hours (Fig. 2B,C).

Often, GBM cells retracted all their processes and assumed a rounded shape, which was followed by the emergence of two lobes, preceding cell division (Fig. 2D, 0 min). During mitosis, on several occasions, a thick structure with a width of several microns formed, and within tens of minutes, when the two GBM cells started to move apart, one to six TMs could be clearly seen (Fig. 2D, 10 min; Movie 1). The TMs formed in this way could be observed for several hours (Fig. 2D). In most cases, TMs formed during mitosis, but we occasionally also observed the formation of TMs following an encounter between two distinct U87 GBM cells (Fig. S1 and Movie 2). During such collisions, the two cells joined very closely, and following this apparent fusion, they separated again, leaving between them connecting TMs. This phenomenon – never observed in normal, healthy neurons – suggests a transient fusion of the cellular membrane of the two GBM cells.

We followed individual TMs for up to 5–6 h, and, at later times, the TMs were usually lost, either because of dye bleaching or because of disruption following the vigorous GBM cell motion. The mean duration of TM persistence in our experimental conditions was 67±7 min, and the TM lengths varied from a few microns to more than 100 µm (Fig. 2F), equivalent to approximately three times the diameter of the GBM cell body. Some TMs extended up to 100–200 µm following GBM cell motion, and some TMs persisted for several hours (Fig. 2E,F).

### $Ca^{2+}$ transients in GBM soma

U87 GBM cells were seeded on 15-mm coverslips at a density of $2.0\times10^4$ cells, and $Ca^{2+}$ transients in their somas were analysed using the $Ca^{2+}$ indicator Fluo-4 AM. GBM cells moved during the $Ca^{2+}$-imaging experiments, and often in 5–10 min, their somas could move by 1–3 µm. Therefore, we analysed $Ca^{2+}$ dynamics only in cells that did not move during the experiment.

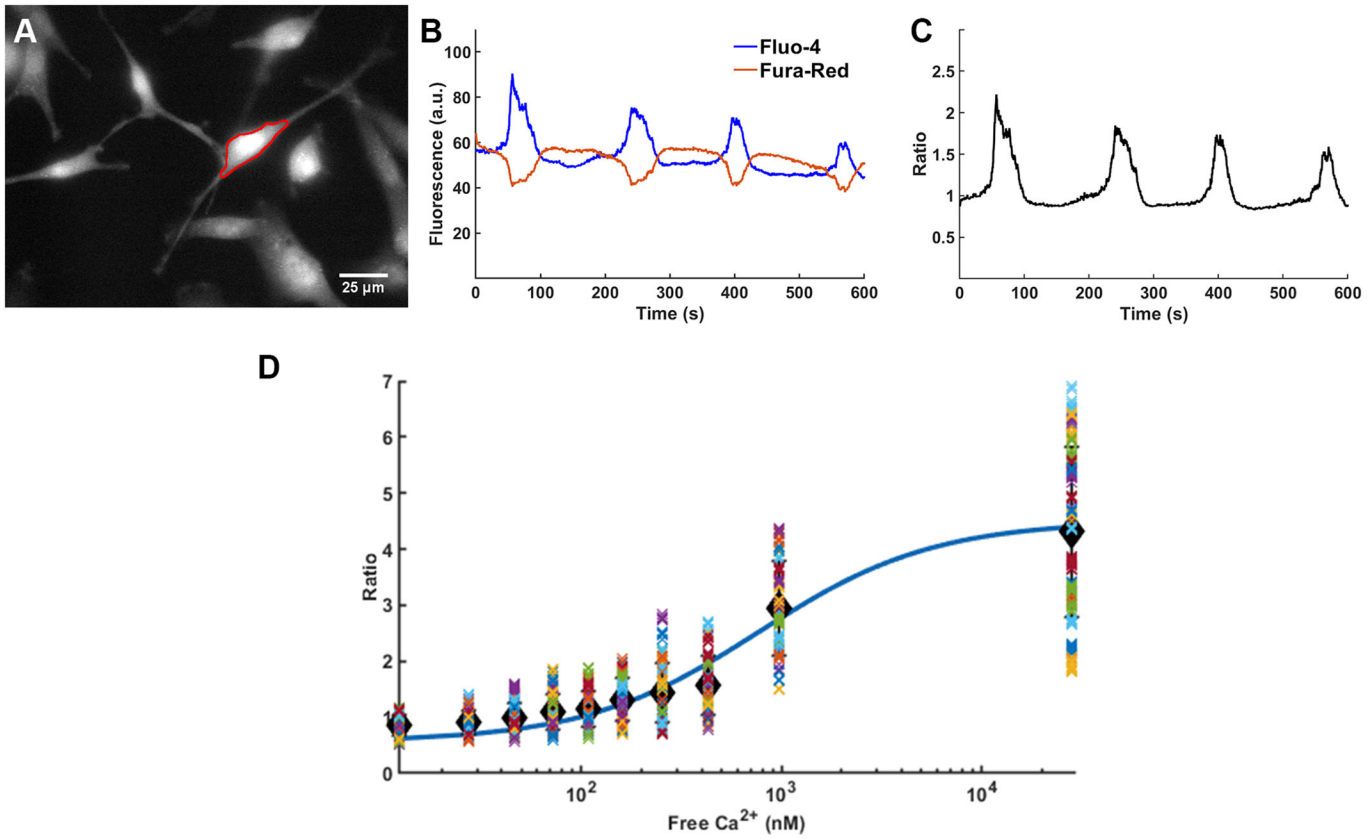


**Fig. 1. $Ca^{2+}$ calibration method.** (A) U87 GBM cells transduced with mCherry. The red outlined area represents a typical region of interest (ROI) used to measure the emitted fluorescence in GBM cells loaded with Fluo-4 AM and Fura Red AM. (B) Time course of the emitted fluorescence by Fluo-4 AM (F1 blue line) and by Fura Red AM (F2 red line) from the ROI of A. The upward and downward signals indicate the optical recordings of the spontaneous $Ca^{2+}$ transients. (C) The fluorescence ratio R obtained from the data shown in B. The amplitude of transients of R=F1/F2 is less affected by dye bleaching than in F1 and F2. (D) Estimation of the parameters used in Eqn 3 to obtain the value of $[Ca^{2+}]_i$ from R. Each coloured dot represents values from a single U87 GBM cell. Data are from 32 different GBM cells in three distinct experimental sessions, and the values obtained for $K_d$, $R_{min}$ and $R_{max}$ are 810.3 nM, 0.56 and 4.60, respectively.

Journal of Cell Science (2020) 133, jcs237503. doi:10.1242/jcs.237503

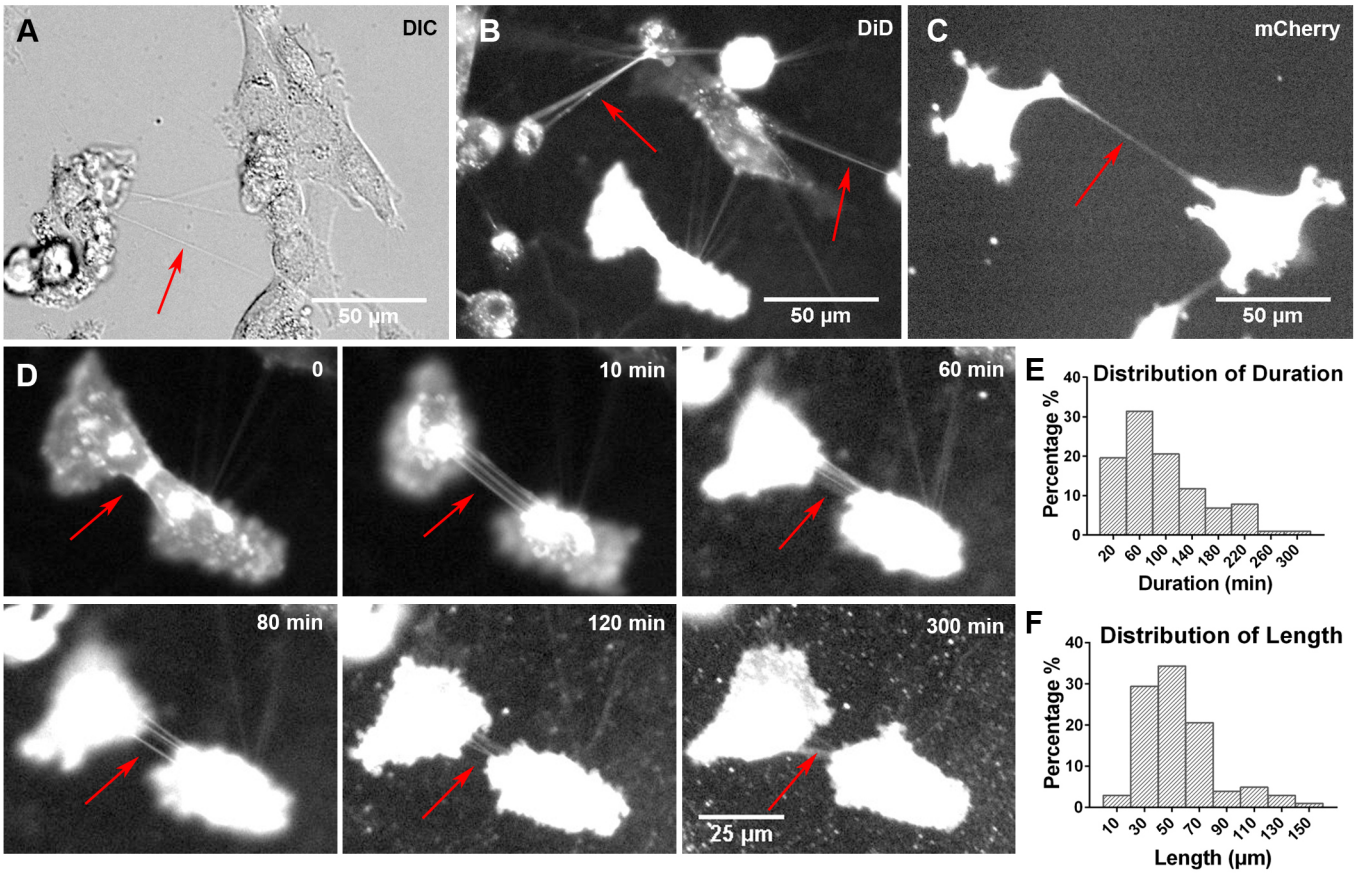


**Fig. 2. Tumour microtubes (TMs) connect U87 GBM cells.** (A) A differential interference contrast (DIC) image of U87 GBM cells. (B) Fluorescence image of U87 GBM cells stained with the fluorescent membrane marker Vybrant™ DiD. (C) Fluorescence image of U87 GBM cells labelled with mCherry. (D) A sequence of fluorescence images of U87 cells stained with Vybrant™ DiD undergoing mitosis. The red arrows in A–D point to TMs, which are more visible when stained by a fluorescent label. (E) Distribution of the durations of TMs. (F) Distribution of the lengths of TMs. The data in E and F were collected from 146 U87 GBM cells in three distinct experimental sessions.

During the first day of culture (Day 1), the great majority of U87 cells remained isolated, and only a small fraction of them was connected by TMs; only occasional $Ca^{2+}$ transients could be detected (Fig. 3A). After culture for 2–3 days (Day 2 and Day 3), more cells had become connected by TMs and had formed a functional network. On Day 2 and Day 3, spontaneous $Ca^{2+}$ waves with durations of ∼1 min could be detected; these waves were almost periodic but exhibited low synchrony (Fig. 3B,C). The amplitude of these optical signals was large, and the value of $DF/F_0$ could exceed 1 (Fig. 3B,C,E). After culture for 4 days (Day 4), the GBM cells had formed a morphologically connected dense layer, and only a few TMs could be detected; the $Ca^{2+}$ transients had become shorter and weaker, with a $DF/F_0$ value less than 0.5 (Fig. 3D,E).

### $Ca^{2+}$ transients in TMs

As represented in Fig. 3E, the properties of the $Ca^{2+}$ transients changed with time after the U87 GBM cells were moved into culture dishes: initially, the cells were isolated, with very few connecting TMs (Day 1), but the fraction of connected cells increased following proliferation (Day 2 and Day 3), and when tumour spheres started to form, the number of visible TMs dropped substantially (Day 4). Similarly, the amplitude and duration of the measured optical transients changed from Day 1 to Day 4 (Fig. 3E), and spontaneous $Ca^{2+}$ waves had a larger amplitude on Day 2 and Day 3 than on Day 1 and Day 4, which suggests that the $Ca^{2+}$ elevation was higher. For these reasons, $Ca^{2+}$ transients were analysed in detail on Day 2 and Day 3.

In several cases, $Ca^{2+}$ transients propagated with a delay varying from 1 to 10 s to a nearby cell, but with a reduced amplitude. In other cases, a small $Ca^{2+}$ transient originating in a distal process was amplified and propagated to the soma. The propagation of $Ca^{2+}$ transients between morphologically connected cells was not always bi-directional, especially in cells connected by TMs (Fig. 4A,C): we often observed the presence of spontaneous localized $Ca^{2+}$ transients in TMs with stereotypical shapes and amplitudes (see orange shading in the red trace in Fig. 4B). However, these transients often did not propagate to the neighbouring portions of the same TM. These experiments were performed with the single $Ca^{2+}$ indicator Fluo-4 AM, and, given the high motility of GBM cells and of the connecting TMs, localized optical transients could be caused by a small motion of the TM itself rather than by a genuine $Ca^{2+}$ hotspot. Therefore, we moved to ratiometric $Ca^{2+}$ imaging based on Fluo-4 AM and Fura Red AM (Assinger et al., 2015); in this method, an increase in $[Ca^{2+}]_i$ causes an increase in the fluorescence emitted by Fluo-4 AM but a decrease in the fluorescence emitted by Fura Red AM (Fig. 1B).

Using ratiometric $Ca^{2+}$ imaging, we determined the complexity of $Ca^{2+}$ propagation along TMs connecting the somas of two GBM cells. Large $Ca^{2+}$ transients originating in the soma of one of the two

Journal of Cell Science (2020) 133, jcs237503. doi:10.1242/jcs.237503

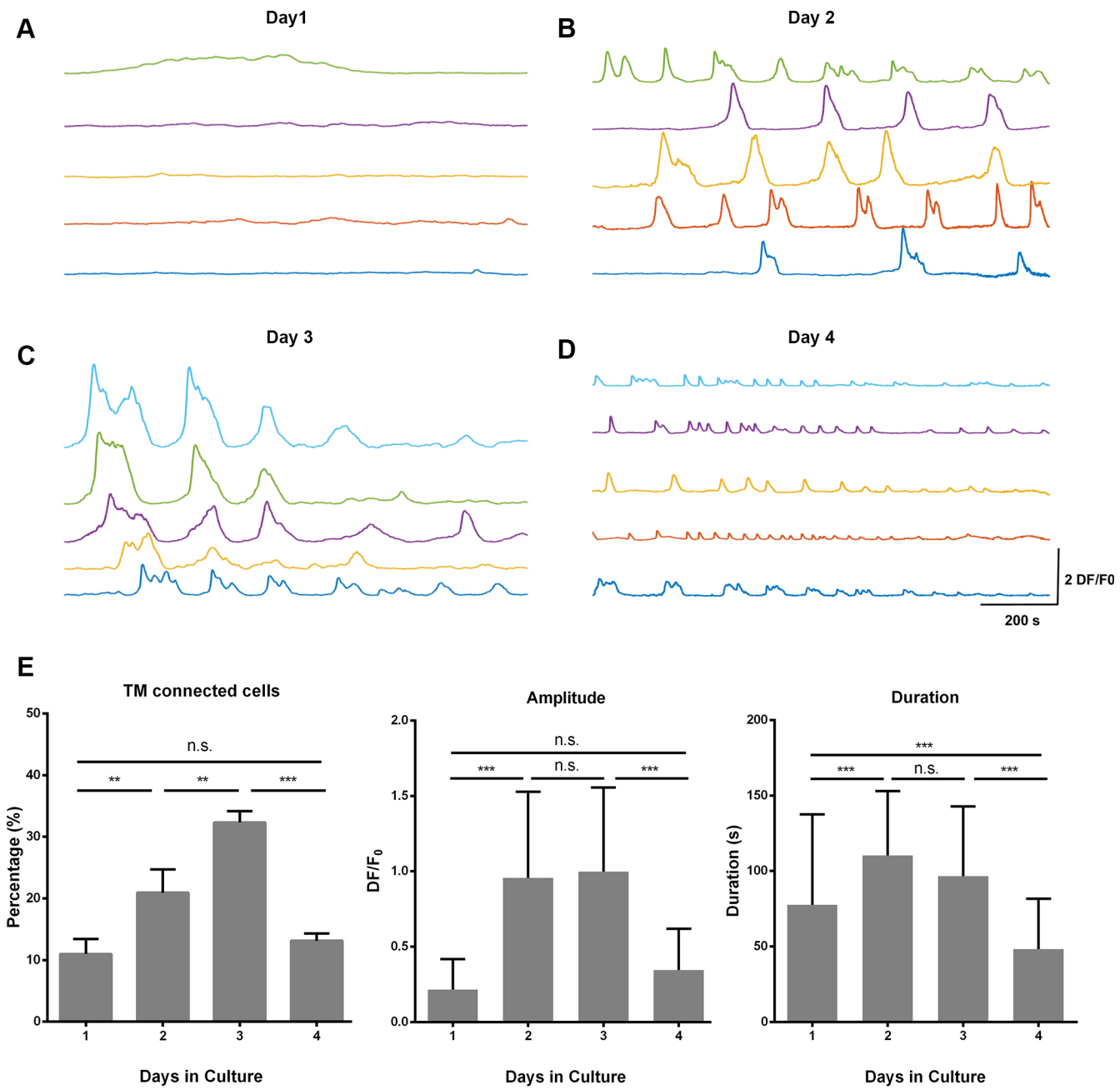


**Fig. 3. Spontaneous $Ca^{2+}$ transients in U87 cells.** (A–D) Optical traces from U87 cells loaded with the $Ca^{2+}$ indicator Fluo-4 AM after cultivation for 1 (A), 2 (B), 3 (C) and 4 (D) days. (E) Distribution of cells connected by TMs (left), amplitude of fluorescent signals during spontaneous optical transients ($DF/F_0$) (middle) and duration of optical transients (right) as a function of days in culture. The data in E were collected from 160 U87 GBM cells in three distinct experimental sessions. The duration of optical transients was measured as the time during which $DF/F_0$ was larger than 0.3 times the peak amplitude of the optical transient. $^{**}P<0.01$, $^{***}P<0.001$. n.s., not significant.

cells propagated along the TM (see the initial large increase in R in the red and blue traces in Fig. 4D). Frequently, following this conventional $Ca^{2+}$ propagation, we observed a $Ca^{2+}$ transient originating in the middle of the same TM that remained localized and did not propagate to the two ends of the TM (see optical transients in the blue trace within the orange shading in Fig. 4D). Similar observations obtained in the other seven TMs suggest that large $Ca^{2+}$ transients originating in GBM cell somas are global events that can invade the entire cell and propagate along the TMs, but small $Ca^{2+}$ transients originating in TMs do not easily propagate and represent localized hotspots.

The presence of $Ca^{2+}$ hotspots along TMs could originate from the presence of local barriers preventing the free diffusion of $Ca^{2+}$. Barriers to free diffusion along TMs could be formed by mitochondria operating in these narrow structures (Bindocci et al., 2017). Therefore, we analysed the presence of mitochondria in the TMs (Fig. 4E) using the dye MitoTracker Red FM (Fig. 4F). We found clear spots of the dye in the middle of TMs, indicating the presence of mitochondria in restricted regions of TMs. These mitochondrial hotspots were also highly dynamic and could move along the TM with a velocity of ∼1 µm/min (compare the 0 min and 15 min images in Fig. 4F; Movie 3).

Journal of Cell Science (2020) 133, jcs237503. doi:10.1242/jcs.237503

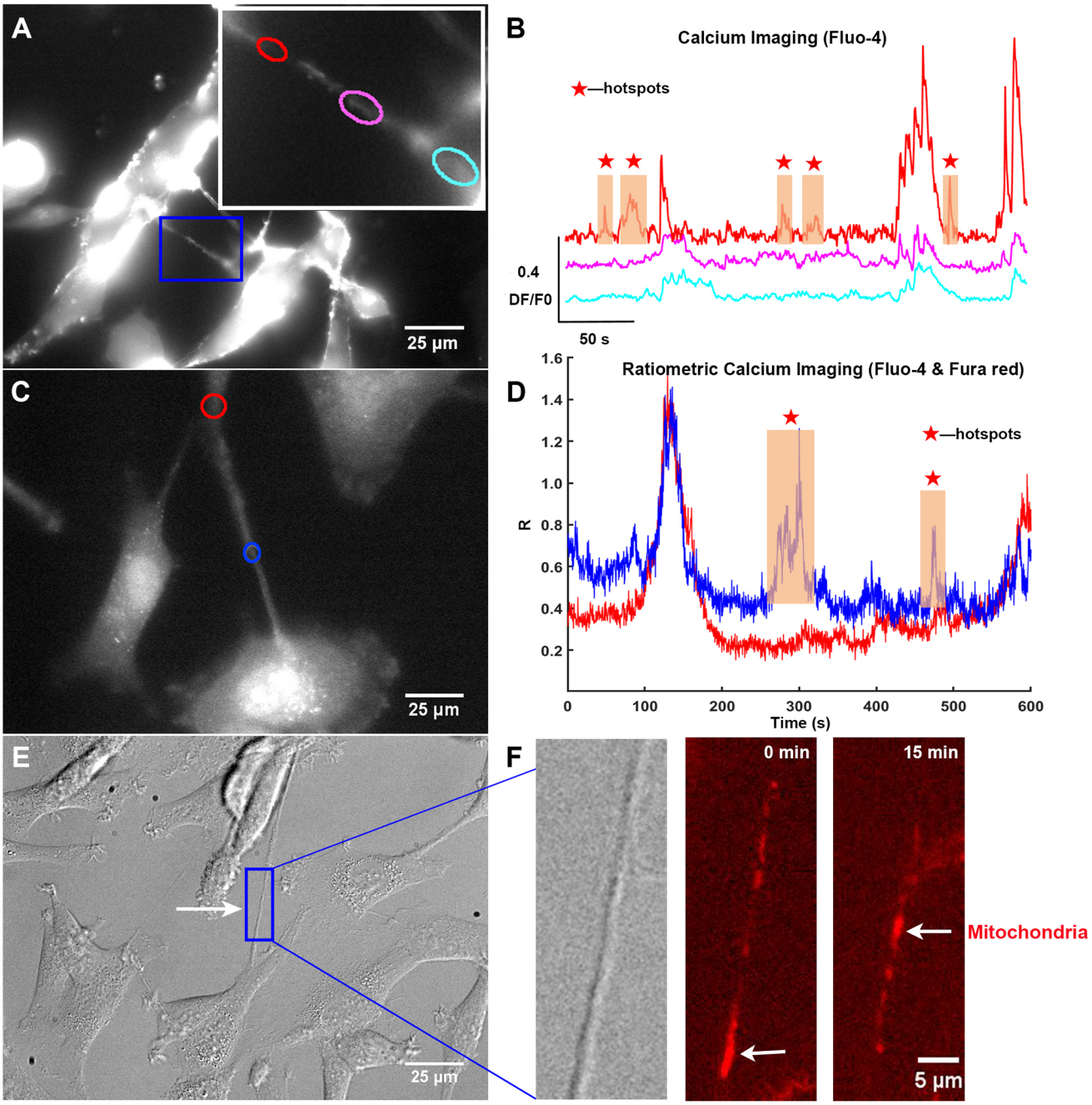


**Fig. 4. Properties of $Ca^{2+}$ transients in TMs.** (A) Fluorescent image of U87 GBM cells loaded with Fluo-4 AM. (B) Optical transients ($DF/F_0$) from the three regions along the TM outlined in colours in A. The red stars indicate the localized optical signals that did not propagate along the TM. (C) As in A, but GBM cells were loaded with both Fluo-4 AM and Fura Red AM to perform ratiometric $Ca^{2+}$ imaging. (D) Time course of R from the red and blue regions shown in C. The initial large optical signal propagated from the red to the blue region, while the optical transients shown in the orange boxes remained confined to the blue region in the middle of the TM. (E) DIC image of a TM connecting two U87 GBM cells, and TM is indicated by an arrow. (F) Magnified images of the staining of mitochondria labelled with MitoTracker Red FM, and mitochondria are indicated by arrows.

### $[Ca^{2+}]_i$ transients reach higher levels in GBM cells than in human astrocytes (HAs)

The use of ratiometric $Ca^{2+}$ imaging not only allows us to verify and rule out possible artefacts caused by cell motion but also enables quantitative estimation of increases in $[Ca^{2+}]_i$ (see Materials and Methods). We examined spontaneous $Ca^{2+}$ waves in HAs (Fig. 5A), U87 cells (Fig. 5B) and GSCs from patients (Fig. 5C) when these cells had formed monolayers in the dishes (Day 2 and Day 3). We often observed global intermittent behaviour in these monolayers: large, synchronous $Ca^{2+}$ transients appeared in most of the visualized cells, but at different times, the $Ca^{2+}$ waves were completely asynchronous. This intermittency between a state with highly synchronous $Ca^{2+}$ waves and a state with randomly occurring $Ca^{2+}$ transients was typical of cells connected by TMs.

In healthy HAs, the spontaneous $Ca^{2+}$ waves reached maximal values below 1 μM (pCa<6 and corresponding to values of R between 2.5 and 3). We never observed $[Ca^{2+}]_i$ elevations above 1 μM in HAs other than those triggering cell death. In U87 cells, the elevation of $[Ca^{2+}]_i$ was much more significant, and the value

Journal of Cell Science (2020) 133, jcs237503. doi:10.1242/jcs.237503

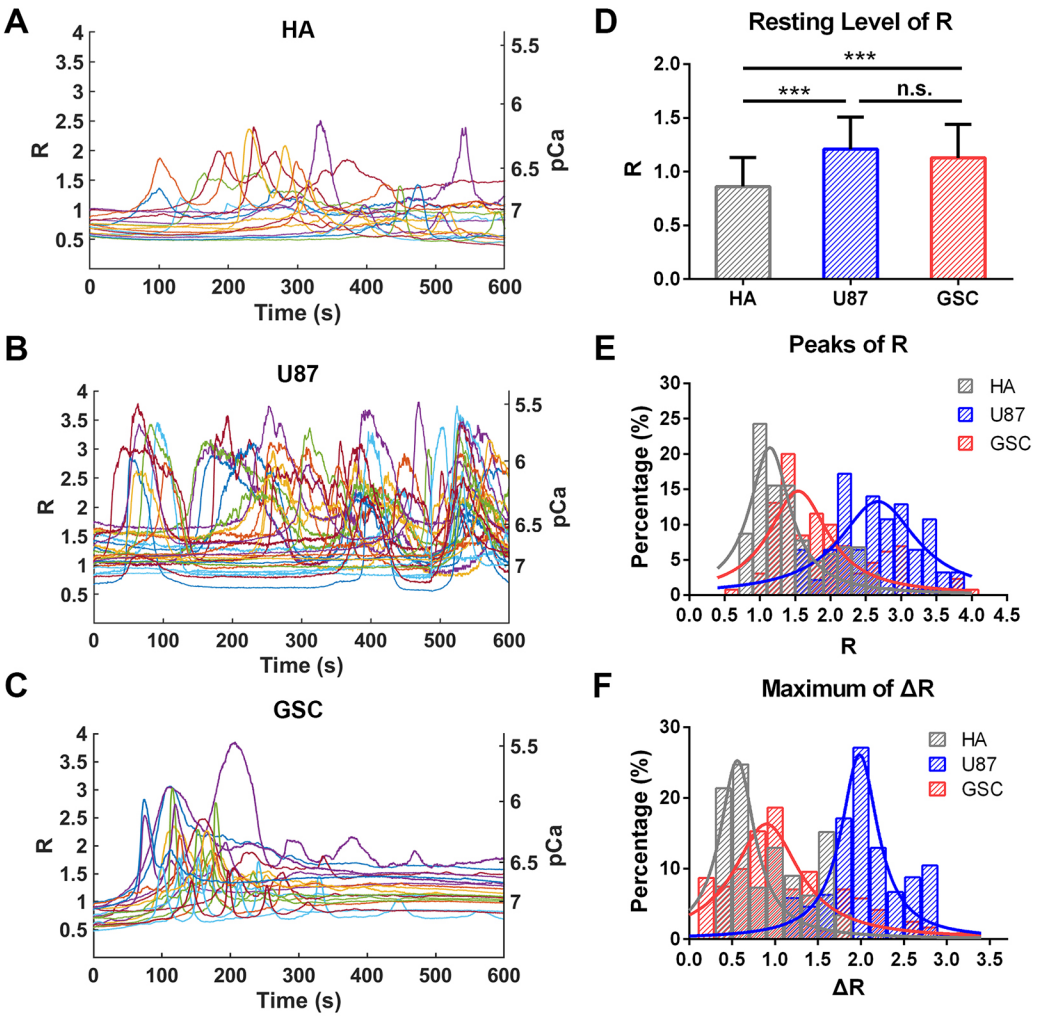


**Fig. 5. Intracellular $Ca^{2+}$ levels in HAs, U87 GBM cells and GSCs from patients.** (A–C) Representative spontaneous intracellular $Ca^{2+}$ waves measured with ratiometric $Ca^{2+}$ imaging in HAs (A), U87 GBM cells (B) and GSCs from patients (C). (D) Average basal values of R in HAs, U87 GBM cells and GSCs. (E) Distribution of the peak values of R during spontaneous $Ca^{2+}$ waves in HAs, U87 GBM cells and GSCs. (F) Distribution of ΔR during spontaneous $Ca^{2+}$ waves in HAs, U87 GBM cells and GSCs. The data in D–F were collected from three distinct experimental sessions. In D, the data represent the mean±s.d. ***$P$<0.001. n.s., not significant.

of R could increase from values of ∼1 to 3.5 and occasionally close to 4 (Fig. 5B). On the basis of the calibration curve (see Fig. 1D), $[Ca^{2+}]_i$ increased to values exceeding 1 µM during the spontaneous $Ca^{2+}$ waves. In GSCs from patients, we observed spontaneous $Ca^{2+}$ waves reaching peak values above 1 µM, and often $[Ca^{2+}]_i$ remained elevated for several minutes (Fig. 5C). Following this unusual $[Ca^{2+}]_i$ elevation, a resting level of ∼100 nM was reached in several minutes without changes in morphology or motility.

Given the uncertainty in estimating the exact value of $[Ca^{2+}]_i$ from R, we compared changes in R and not in $[Ca^{2+}]_i$ in different cell types. The mean resting level of R was close to 1 in HAs and slightly greater in U87 cells and GSCs (Fig. 5D). The change in R (ΔR) and the maximal value of R at the peak of the spontaneous $Ca^{2+}$ waves were significantly higher in U87 GBM cells than in HAs or GSCs (Fig. 5E,F). Both ΔR and the peak values of R were higher in GSCs than in HAs, but to a lesser extent. Based on these results, we conclude that $[Ca^{2+}]_i$ in U87 cells and in GSCs from patients can reach levels much higher than those in HAs without causing any signs of cell death.

### Comparison of the expression of MCU in HAs, U87 GBM and GSCs

There are several indications that $Ca^{2+}$ regulation and homeostasis are different in cancer cells than in normal healthy cells, particularly in glioma and GBM (Farfariello et al., 2015; Marchi and Pinton, 2016). Indeed, a recent bioinformatics analysis (Robil et al., 2015) identified higher levels of expression of several genes related to $Ca^{2+}$, which were collectively referred to as the $Ca^{2+}$ toolbox, in cancer cells. This toolbox contains several tens of genes, some of which could be involved in helping GBM cells to sustain higher levels of $[Ca^{2+}]_i$ than those in other cells: a gene that is highly expressed in GBM cell lines but expressed at lower levels in normal brain tissues is *MCU*. In addition, some proteins of the S100 family of $Ca^{2+}$-binding proteins are overexpressed in brain tumours; namely, S100A2, S100A4, S100A8 and S100A11, and have been reported as markers of tumorigenicity (Rand et al., 2008). Therefore, we used western blotting and immunofluorescence to verify whether the overexpression of MCU could be responsible for the resistance and tolerance of GBM cells to unusual elevation of $[Ca^{2+}]_i$ (Fig. 6).

Journal of Cell Science (2020) 133, jcs237503. doi:10.1242/jcs.237503

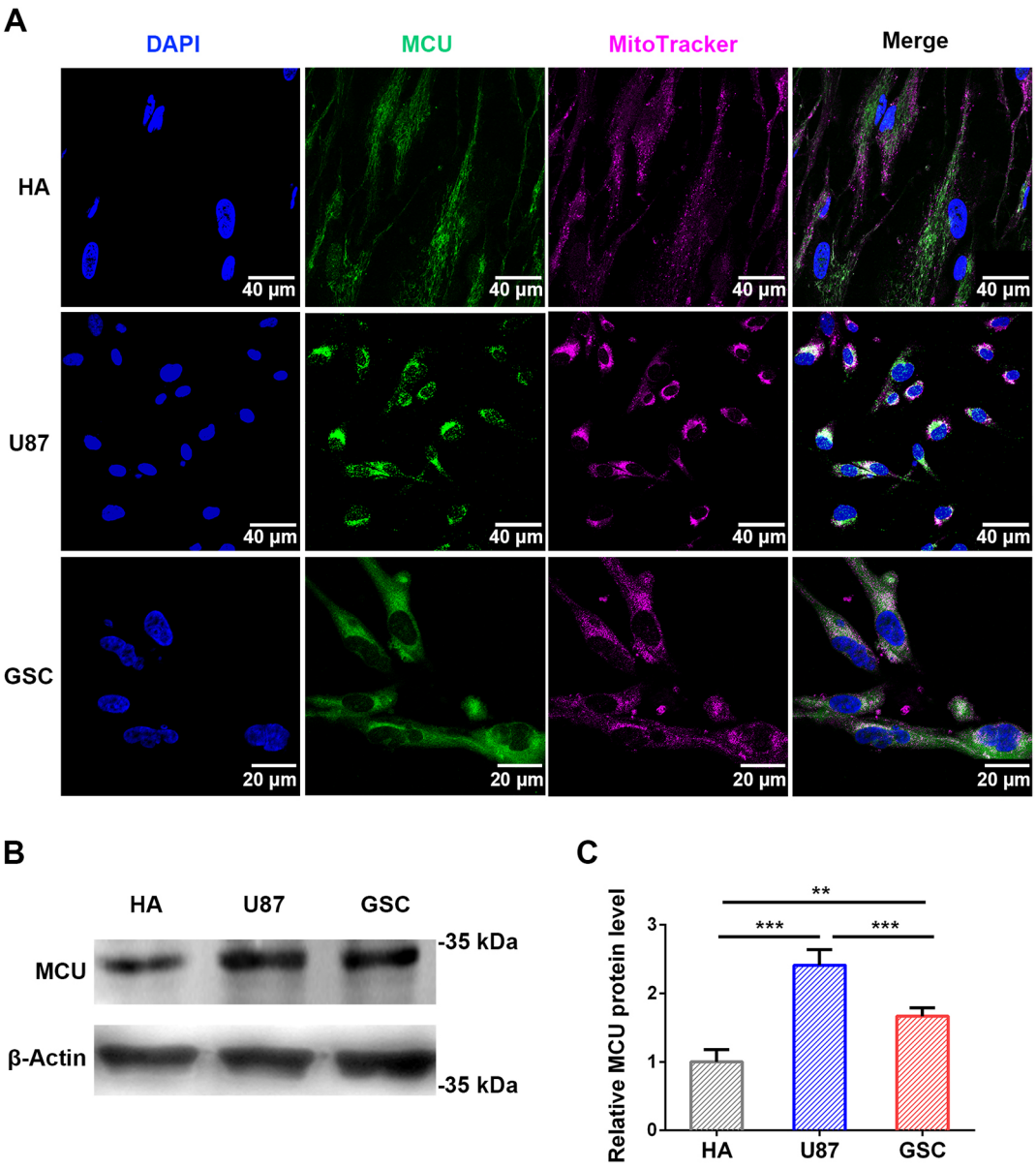


**Fig. 6. The mitochondrial $Ca^{2+}$ uniporter (MCU) in HAs, U87 GBM cells and GSCs from patients.** (A) Representative confocal images showing the expression of MCU in HAs, U87 GBM cells and GSCs from patients; MitoTracker Red was used to identify mitochondria. (B) Western blot showing MCU expression in HAs, U87 GBM cells and GSCs. (C) MCU quantification using β-actin as a housekeeping protein. The data are from three distinct experimental sessions and represent the mean±s.d. $^{**}P<0.01$, $^{***}P<0.001$.

Immunofluorescence analysis showed vigorous staining for MCU in HAs, U87 GBM cells and GSCs from patients (Fig. 6A). Co-staining with the mitochondrial marker MitoTracker Red indicated a strong colocalization, confirming MCU localization in the mitochondria. Moreover, western blot analysis showed that the relative expression level of MCU in U87 cells was approximately twice that observed in HAs (Fig. 6B,C). In GSCs from patients, the expression level of MCU was also higher than that in HAs, but to a lesser extent.

### MCU expression level influences $[Ca^{2+}]_i$ and cell proliferation

A key question is the source of the observed $Ca^{2+}$ transients: does the rise in $[Ca^{2+}]_i$ originate from the extracellular medium or is it released from internal stores, such as mitochondria? Therefore, we analysed $Ca^{2+}$ waves in U87 GBM and HA cells following the removal of extracellular $Ca^{2+}$. The cells were treated with a $Ca^{2+}$-free Dulbecco's modified Eagle medium (DMEM) and ratiometric $Ca^{2+}$ imaging was performed at different time points. In U87 GBM cells, following 1 h of $Ca^{2+}$-free treatment, the $Ca^{2+}$ waves started to decrease in frequency (compare Fig. 7A and B), while the basal level of R decreased from a mean value of ∼1 to 0.6 (Fig. 7G), corresponding to a drop in $[Ca^{2+}]_i$ from 100 nM to 10 nM. After 4 h, only occasional $Ca^{2+}$ waves could be seen (Fig. 7C), and the basal level of $[Ca^{2+}]_i$ dropped to less than 10 nM. In HAs, the trend was consistent: following $Ca^{2+}$-free treatment the frequency of $Ca^{2+}$ waves (Fig. 7D–F) and the basal level of R decreased (Fig. 7H). These observations suggest that internal $Ca^{2+}$ stores are very efficient, and for several hours, they are an alternative source to the extracellular medium as a $Ca^{2+}$ reservoir.

Next, we analysed the effects of *MCU* silencing on U87 GBM cells, and *MCU* overexpression on HAs, after transfection with short hairpin RNA (shRNA) for MCU (sh-MCU) and pDEST40-MCU-

Journal of Cell Science (2020) 133, jcs237503. doi:10.1242/jcs.237503

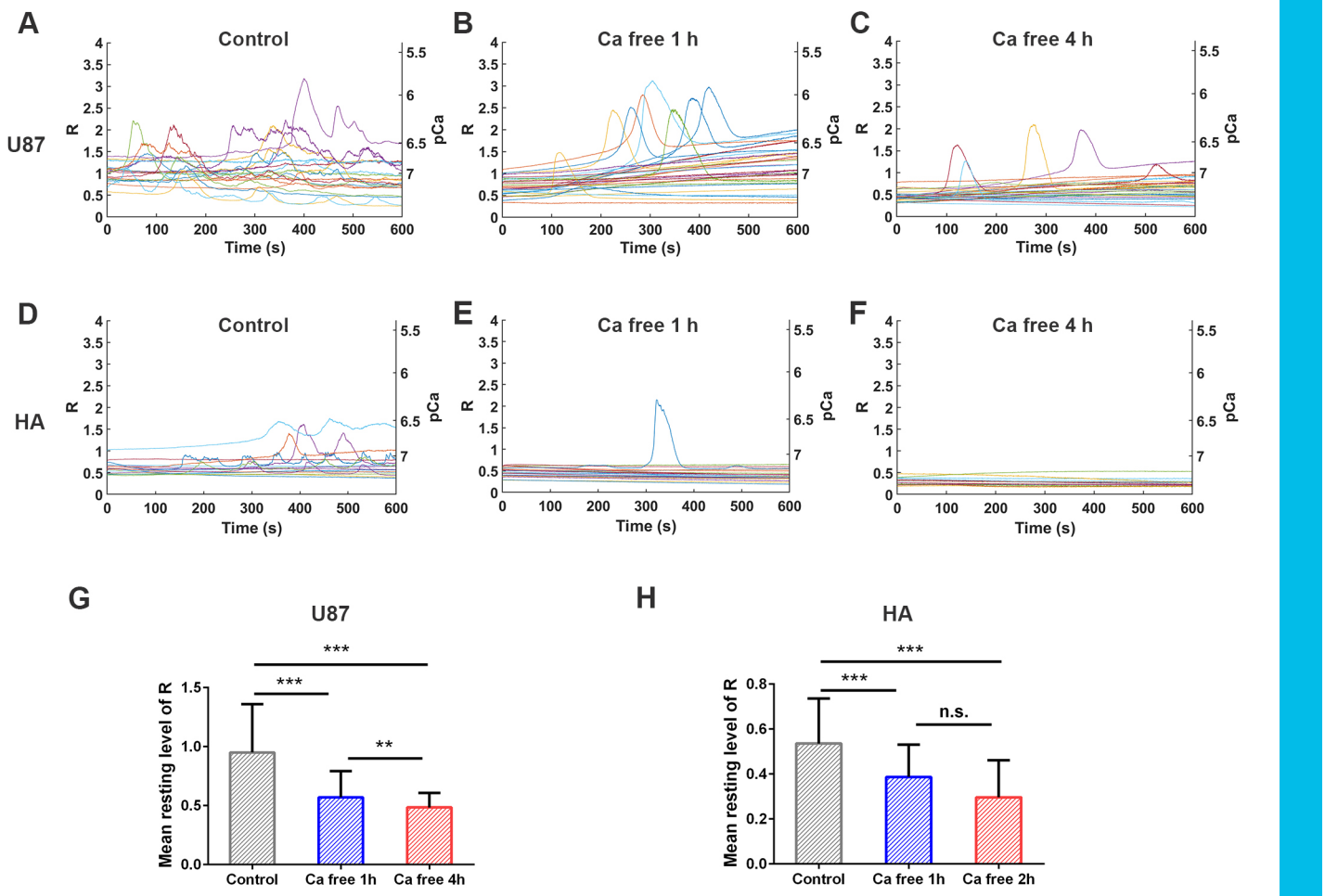


**Fig. 7. The removal of extracellular $Ca^{2+}$ reduced $Ca^{2+}$ transients and $[Ca^{2+}]_i$ in U87 GBM and HA cells.** (A–F) Representative spontaneous intracellular $Ca^{2+}$ waves measured with ratiometric $Ca^{2+}$ imaging in U87 GBM and HA cells in the control (A,D) or $Ca^{2+}$-free (B,C,E,F) medium. (G,H) Average basal values of R in U87 GBM (G) and HA (H) cells. The data in G and H are from three distinct experimental sessions and represent the mean±s.d. ***P*<0.01, ****P*<0.001. n.s., not significant.

V5-HIS, respectively. We observed that, 48 h after transfection, MCU expression in U87 GBM cells was reduced by 70% in the sh-MCU group (Fig. 8A) compared to what was measured in the non-target shRNA vector as a negative control (sh-NC) group, whereas it increased by 90% in HAs (Fig. 8B) compared to what was measured in the control cells.

Since MCU level influences the dynamics of spontaneous $Ca^{2+}$ waves, we performed ratiometric $Ca^{2+}$ measurements and compared the data obtained from U87 GBM to those obtained from HAs under control conditions, and to those from cells after silencing or overexpression of *MCU*. After these treatments, spontaneous $Ca^{2+}$ waves were still present in HAs and U87 GBM cells. Following *MCU* silencing or overexpression, the mean basal level of R was not influenced in U87 GBM cells or in HAs (Fig. 8C). *MCU* silencing caused a decrease in the mean peak R in U87 GBM from a value of ∼2.5 to 2 (Fig. 8D), corresponding to a decrease in $[Ca^{2+}]_i$ from 700 nM to 400 nM. The mean peak R in HAs increased from a value of ∼1 to 1.5 after *MCU* overexpression (Fig. 8D). Previously, it was reported that cytoplasmic $Ca^{2+}$ peaks were reduced or enhanced by *MCU* overexpression and silencing in cardiomyocytes, respectively (Drago et al., 2012), whereas the opposite occurs within the mitochondrial matrix. Differences between Drago et al.'s findings and our results are likely caused by the fact that our ratiometric $Ca^{2+}$-imaging experiments were based on measuring the fluorescence emitted from the whole GBM, without distinguishing among the different intracellular compartments. Therefore, we performed ratiometric $Ca^{2+}$-imaging experiments with U87 GBM cells stained with Fluo-4 AM, Fura Red AM and MitoTracker Red (Fig. S2A), and analysed $Ca^{2+}$ waves in nucleus, mitochondria and cytoplasm, as described in Fig. S2. After *MCU* silencing in U87 GBM, during $Ca^{2+}$ waves the peak R in mitochondria decreased significantly (Fig. S2B), which is consistent with Drago et al.'s conclusion, and the peak R was slightly decreased in the nucleus and slightly increased in the cytoplasm. In HAs we did not observe any significant difference in the compartments following *MCU* overexpression (Fig. S2C).

To test the effect of MCU on proliferation, we plated the same numbers of HAs and U87 cells in 96-well plates and analysed the proliferation rate using the alamarBlue® cell viability assay (see Materials and Methods). Two days after transfection, the proliferation rate was reduced by 15% in U87 GBM cells, and by 20% in HAs (Fig. 8E). These results show that both *MCU* silencing in U87 GBM cells and *MCU* overexpression in HAs significantly reduce cell proliferation. In order to understand if the reduced proliferation is associated with cell death, we carried out fluorescence-activated cell sorting (FACS) analysis. In particular, we used co-staining with Annexin V and propidium iodide (PI) to quantify live, early apoptotic, late apoptotic and necrotic cells (Fig. 8F). The percentage of dead cells and types of cell death were

Journal of Cell Science (2020) 133, jcs237503. doi:10.1242/jcs.237503

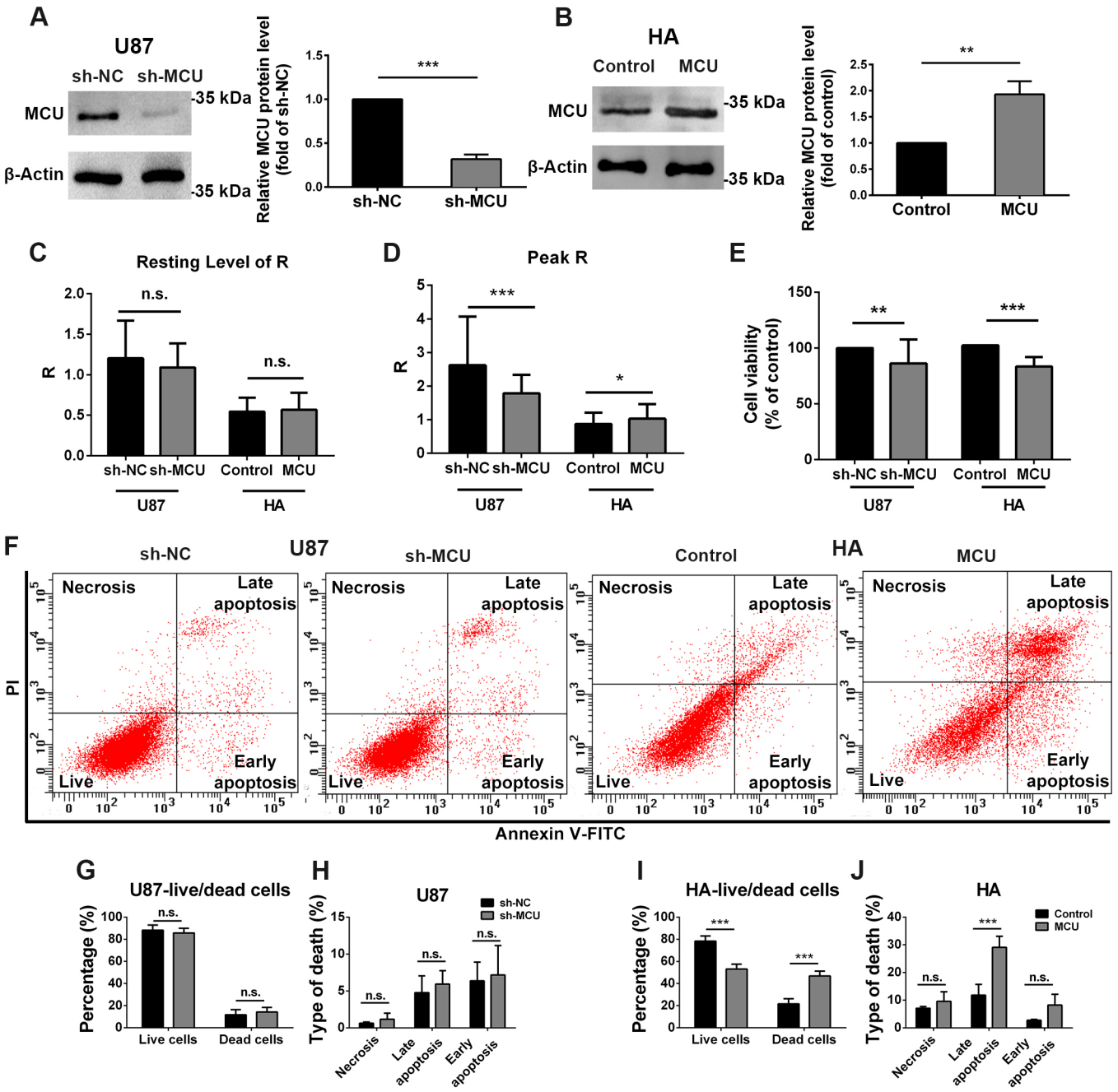


**Fig. 8. The effects of the MCU expression level on U87 GBM and HA cells.** (A,B) MCU expression was detected by western blotting (left) and relative protein levels were quantified (right) in U87 GBM cells after *MCU* silencing (A) and in HAs after *MCU* overexpression (B). (C,D) Average basal values of R (C) and peak R (D) in U87 GBM cells and HAs after transfection for 48 h. (E) Results from alamarBlue® cell viability assay in U87 GBM cells and HAs after transfection. (F) Representative dot plots of U87 GBM cells and HAs after transfection and staining for Annexin V and PI. (G,H) Fraction of live and dead cells in U87 GBM (G) and HA (H) cells. (I,J) Fraction of cells in necrosis, late apoptosis and early apoptosis in U87 GBM (I) and HA (J) cells. The data are from three distinct experimental sessions and represent the mean±s.d. **P*<0.05, ***P*<0.01, ****P*<0.001. Control, empty vector control; MCU, vector-expressing MCU; n.s., not significant; sh-MCU, shRNA targeting MCU; sh-NC, shRNA negative control.

not significantly different between the sh-MCU group of U87 GBM cells after *MCU* silencing and the sh-NC group (Fig. 8G,H). Interestingly, dead cells increased instead from 20% to 45% in HAs following *MCU* overexpression, and the cell death was mainly due to late apoptosis (Fig. 8I,J).

Taken together, these results suggest that *MCU* silencing in U87 GBM decreases spontaneous $Ca^{2+}$ oscillations and cell proliferation without triggering cell death. Conversely, *MCU* overexpression in HAs slightly increases $Ca^{2+}$ levels but causes cell death, suggesting that HAs cannot tolerate high MCU levels.

## DISCUSSION

$Ca^{2+}$ is an intracellular second messenger controlling fundamental cellular processes, such as gene transcription, cell cycle regulation and cell proliferation, and an overload of $[Ca^{2+}]_i$ triggers cell death (Zhivotovsky and Orrenius, 2011). The present investigation

illustrates three novel observations regarding $Ca^{2+}$ regulation in GBM cells: first, $Ca^{2+}$ waves were propagated in networks of cells connected by TMs in a complex way with variable directions and modes; second, in the U87 GBM cell line and in GSCs from patients, the basal level of $[Ca^{2+}]_i$ was ∼100 nM, but, during spontaneous waves, $[Ca^{2+}]_i$ reached an unusual high level above 1 µM for long periods without triggering cell death; and third, the levels of a protein involved in mitochondrial $Ca^{2+}$ regulation, MCU, was altered in GBM cells compared to healthy HAs. Moreover, our analysis shows that *MCU* silencing decreases cell proliferation and alters $[Ca^{2+}]_i$ dynamics in U87 GBM cells, and *MCU* overexpression in HAs increases $[Ca^{2+}]_i$, inducing also cell death. Our findings delineate an interplay between the high level of MCU, large unusual $[Ca^{2+}]_i$ and proliferation ability, which is a potential factor in GBM malignancy, possibly caused by activation of the $Ca^{2+}$-calmodulin complex, CaMKII and specific transcription factors regulated by $[Ca^{2+}]_i$, such as the CREB family members (Shanmughapriya et al., 2015). Indeed, a sustained activation of CaMKII and CREB have been demonstrated to promote proliferation (Steven and Seliger, 2016).

### $Ca^{2+}$ signalling and propagation along TMs

$Ca^{2+}$ propagation along TMs connecting different GBM cells is characterized by the occurrence of hotspots, where spontaneous increases in $[Ca^{2+}]_i$ remain localized and do not propagate (Fig. 4). These hotspots were observed with the common $Ca^{2+}$ dye Fluo-4 AM (Fig. 4A,B) and were confirmed by ratiometric $Ca^{2+}$ imaging (Fig. 4C,D). Similar $Ca^{2+}$ hotspots have also been observed in fine neurites of healthy astrocytes (Bindocci et al., 2017), and the existence of these hotspots requires the existence of functional barriers at their borders. These barriers are likely to be composed of buffering organelles, such as mitochondria and/or $Ca^{2+}$ buffers, i.e. proteins acting as local $Ca^{2+}$ sinks (Schwaller, 2010). These buffers can be quickly saturated, and, under these circumstances, the barriers do not operate and will allow $Ca^{2+}$ waves to propagate freely. Mobile mitochondria are the most likely candidates for this role (Agarwal et al., 2017; Jackson and Robinson, 2015), and their presence (see Fig. 4F) in TMs explains the observed behaviour. A propagating large $Ca^{2+}$ wave will saturate the $Ca^{2+}$-buffering capacity of mitochondria and be likely to diffuse (Fig. 4B,D), while a small $Ca^{2+}$ hotspot originating in the middle of a TM will remain confined in the TM because the diffusing $Ca^{2+}$ will be completely absorbed by the mitochondria.

It is important to observe that propagation of $Ca^{2+}$ transients in the soma and along TMs is different: $Ca^{2+}$ transients within the soma of GBM propagate easily while $Ca^{2+}$ transients can be blocked along TMs and fine GBM neurites. This different behaviour is a consequence of the presence of buffering organelles in TMs (Fig. 4F), where mobile mitochondria can block $Ca^{2+}$ transients, which does not occur in GBM soma because of their larger size.

Assemblages of GBM cells appear to function as groups of elements with variable coupling, leading to an intermittent behaviour in which synchronous $Ca^{2+}$ waves are interspersed with asynchronous $Ca^{2+}$ waves. This intermittent behaviour can be seen within different compartments present in the same cell or in networks of cells.

### Unusual elevation of $[Ca^{2+}]_i$ during spontaneous waves

Changes in $[Ca^{2+}]_i$ can be quantified by using ratiometric $Ca^{2+}$ dyes such as Fura-2 (Harley et al., 2010; Shin et al., 2018) or using two dyes with different emission wavelengths, such as Fluo-4 AM and Fura Red AM (Assinger et al., 2015). These procedures enable quantitative determination of $[Ca^{2+}]_i$, but a caveat must be recognized: the calibration procedure to transform the measured ratio into absolute $[Ca^{2+}]_i$ could be affected by the presence of intracellular compartments and is less accurate for $[Ca^{2+}]_i$ exceeding ∼1 µM than for lower levels. Therefore, we did not determine the exact highest $[Ca^{2+}]_i$ reached during the spontaneous waves but estimated it to be in the order of 3–5 µM.

It is commonly accepted that, at steady state, the basal level of $[Ca^{2+}]_i$ is determined by $Ca^{2+}$ influx and extrusion through the plasma membrane and is independent of the intracellular buffering capacity, i.e. the capacity of mitochondria and other organelles able to sequester and release $Ca^{2+}$. However, a large buffering capacity prolongs the time taken to reach the steady state and introduces unexpected dynamics. In U87 GBM and HA cells, large $Ca^{2+}$ waves were observed for 1–2 h after removal of extracellular $Ca^{2+}$, indicating that, in cells, mitochondria and other organelles are excellent sources and sinks of $Ca^{2+}$.

These observations suggest a complex origin and control of $Ca^{2+}$ transients: indeed the observation that large $Ca^{2+}$ transients are observed even following removal of extracellular $Ca^{2+}$ for 1 h (Fig. 7B,E) indicates that the release of $Ca^{2+}$ from intracellular stores contribute to the large $Ca^{2+}$ transients. Prolonged removal of extracellular $Ca^{2+}$ – for more than 4 h – abolishes most of these transients (Fig. 7C,F), suggesting that extracellular $Ca^{2+}$ plays an important role. Therefore, these transients have a dual and complex origin, i.e. release form intracellular stores and entry from the extracellular medium likely through $Ca^{2+}$-permeable ionic channels.

There is agreement that basal $[Ca^{2+}]_i$ varies between 100 nM and 300 nM in different cells and that changes in $[Ca^{2+}]_i$ underlie fundamental biological processes. For example, during phototransduction in vertebrate photoreceptors, $[Ca^{2+}]_i$ decreases, and this drop is responsible for light adaptation (Krizaj and Copenhagen, 2002); in addition, local increases in $[Ca^{2+}]_i$ are required for transmitter release at synapses (Koch and Dell'orco, 2013). Relatively small increases in $[Ca^{2+}]_i$ can be beneficial to cells by promoting the mitochondrial $Ca^{2+}$ uptake machinery and thus making it more efficient (Basso et al., 2018). When $[Ca^{2+}]_i$ increases above the micromolar level, cell death can be initiated (Tombal et al., 2002). The precise dangerous level of $[Ca^{2+}]_i$ varies in different cell types, and the mechanisms through which elevation of $[Ca^{2+}]_i$ promotes cell death include activation of $Ca^{2+}$-dependent proteases, nitric oxide synthases, the CREB family of $Ca^{2+}$-dependent transcription factors, caspases and calpain proteins (Caro and Cederbaum, 2002; Teich et al., 2015). The $Ca^{2+}$ sensitivity of many of these proteins is in the micromolar range (Caro and Cederbaum, 2002); for this reason, to avoid triggering cell death, it is important to limit sustained increases in $[Ca^{2+}]_i$ to below 1 µM.

As shown in Fig. 5, in U87 GBM cells and in GSCs from patients, $[Ca^{2+}]_i$ increased above 1 µM without leading to cell death. Conversely, overexpression of *MCU* in HAs increased $[Ca^{2+}]_i$ and led to cell death (Fig. 8I). These results suggest that GBM cells might have molecular mechanisms that enable them to accommodate large increases in $[Ca^{2+}]_i$, implying the existence of a larger pool of intracellular buffering organelles or $Ca^{2+}$-buffering proteins in GBM cells than in normal cells. These mechanisms could be complemented by an efficient mechanism of $Ca^{2+}$ extrusion, and the overexpression of key anti-apoptotic signals (Ziegler et al., 2008), such as members of the BCL2 family (Belmar and Fesik, 2015), that inhibit the activity of caspase-3, caspase-7 and caspase-9.

### The role of MCU in $Ca^{2+}$ transients

Greater mitochondrial buffering capacity caused by higher levels of MCU could have contributed to the presence of $Ca^{2+}$ hotspots along TMs and the unusual levels of $[Ca^{2+}]_i$ observed in GBM cells compared to normal cells during the spontaneous $Ca^{2+}$ waves. One way to rapidly neutralize transient elevations in $[Ca^{2+}]_i$ is by sequestering the $Ca^{2+}$ into various intracellular stores of $Ca^{2+}$, such as those in the endoplasmic reticulum (ER) and the $Ca^{2+}$ matrix inside the mitochondria. MCU plays a key role in sequestering $[Ca^{2+}]_i$ by promoting $[Ca^{2+}]_i$ accumulation in the mitochondrial matrix, and mitochondrial $Ca^{2+}$ elevation favours drug resistance and tumour maintenance in cancer cells (Vultur et al., 2018). MCU is characterized by a low $Ca^{2+}$ affinity [dissociation constant (KD)=20–30 µM] and is normally closed. However, when surrounding $Ca^{2+}$ levels are high enough to form high-$[Ca^{2+}]_i$ (∼10 µM) microdomains in close proximity to the mouth of the ER, MCU can be activated to take up $Ca^{2+}$ into mitochondria (Arruda and Hotamisligil, 2015; Villalobos et al., 2017). Upregulation of MCU has been demonstrated in different cancers, such as breast cancer (Hall et al., 2014) and hepatocellular carcinoma (Ren et al., 2018), and *MCU* silencing can reduce mitochondrial $Ca^{2+}$ uptake and metastatic cell motility and potentiate cell death, suggesting that *MCU* overexpression protects cancer cells from apoptosis (Curry et al., 2013; Tosatto et al., 2016).

An elevated level of $[Ca^{2+}]_i$ is expected to activate several transcription factors involved in the regulation of cell division and proliferation, such as the CREB family (Shanmughapriya et al., 2015). In GBM cells, the spontaneous $Ca^{2+}$ waves started from a basal level of ∼100 nM and reached a peak at 1–3 µM or higher. Following *MCU* silencing, spontaneous $Ca^{2+}$ waves were still present and GBM cells had reduced proliferation. These findings indicate that the spontaneous $Ca^{2+}$ waves from 100 nM to 1–3 µM or higher could be responsible for the high proliferation in GBM cells. Therefore, the key hallmark of GBM malignancy, abnormal rate of proliferation, is caused – to some extent – by the observed high MCU level and unusual elevation of $[Ca^{2+}]_i$.

In addition, *MCU* transcription is controlled by the CREB transcription factors and CREB binding to the *MCU* promoter, which is regulated by $[Ca^{2+}]_i$. Therefore, we can deduce that, in GBM, there is also a positive feedback between the level of MCU and spontaneous $Ca^{2+}$ transients.

### Conclusions

In conclusion, our study elucidates how high MCU level and large $Ca^{2+}$ transients are linked to malignancy in GBM. Indeed, an unusual elevation of $Ca^{2+}$ transients is expected to activate biochemical pathways involved in cell proliferation, the key hallmark of GBM malignancy. Since cell proliferation is reduced when MCU is silenced, targeting the MCU complex and intracellular $Ca^{2+}$ regulation could be a new unexplored strategy for the treatment of GBM.

## MATERIALS AND METHODS

### Cell culture

HAs (#N7805100, Thermo Fisher Scientific) and U87 GBM cells (#89081402, Sigma-Aldrich) were cultured in DMEM supplemented with 10% fetal bovine serum (FBS; Invitrogen, Life Technologies, Gaithersburg, MD), 1% PenStrep (100 U/ml penicillin and 100 µg/ml streptomycin; Invitrogen). For HAs, 1% N-2 Supplement (Thermo Fisher Scientific) was added to the culture medium and all plates used to culture HAs were covered with Geltrex™ matrix (Thermo Fisher Scientific). The mCherry-labelled U87 GBM cells were kindly provided by Prof. Antonello Mallamaci (Neurobiology Sector, International School for Advanced Studies, Trieste, Italy). U87 GBM cells were acutely infected at a concentration of 500 cells/µl by a mix containing lentiviral vector, LV_Pgk1p-mCherry, at a multiplicity of infection of 6.

To obtain human GSCs, human GBM samples were collected by the Neurosurgery Department of the Azienda Ospedaliera Universitaria of Udine, after informed consent was obtained, in accordance with the Declaration of Helsinki, and with approval by the Independent Ethics Committee of the University Hospital of Udine (Approval 196/2014Em). Human GSCs were expanded in adherent culture following the protocol optimized by Dirk's group to maintain undifferentiated GSCs in adherent condition (Andolfi et al., 2014; Bourkoula et al., 2014; Pollard et al., 2009). Briefly, tissue samples were mechanically enzymatically dissociated and single-cell suspensions were cultured with adhesion on laminin-coated dishes in a growing medium composed of the following: Neurobasal™-A Medium (#10888, Gibco by Invitrogen) supplemented with 2 mM L-glutamine (#G7513, Sigma-Aldrich), 1× N2 supplement [7.5% bovine serum albumin (BSA), 0.63 µg/ml progesterone, 1.6 mg/ml putrescine dihydrochloride, 0.52 µg/ml sodium selenite], 25 µg/ml insulin (#I2643, Sigma-Aldrich), 1× penicillin-streptomycin (#15140122, Gibco by Invitrogen), 100 µg/ml h-apo-transferrin (#P4333, Sigma-Aldrich), 1× B-27 supplement (#17504-044, Gibco by Invitrogen), 20 ng/ml h-FGF-basic (#100-18B, Peprotech), 20 ng/ml h-EGF (#AF-100-15, Peprotech).

All the cells were cultured in an incubator at 37°C, 5%$O_2$/5% $CO_2$, 95% relative humidity and medium was replaced every 3 days. Once 70–80% of confluence had been reached, the cells were re-plated at a density of $2.5\times10^3/cm^2$.

### Transfection

pDEST40-MCU-V5-HIS was Addgene plasmid #31731, deposited by Vamsi Mootha, and sh-MCU was obtained from Sigma-Aldrich (#SHCLNG-NM_138357). Twenty-four hours after plating the cells, HA cells were transfected with pDEST40-MCU-V5-HIS using the empty vector as a control; U87 GBM cells were transfected with sh-MCU using non-target shRNA vector as a negative control (sh-NC). Lipofectamine 3000® transfection reagent (Invitrogen) was used following the manufacturer's protocol. Forty-eight hours after transfection, the following tests were carried out.

### Live-cell imaging

Cells were plated at a density of $8.0\times10^4$ cells into 35-mm dishes with a glass bottom and cultured for 2 days. Before optical recording, cells were stained with 5 µl/ml Vybrant™ DiD Cell-Labelling Solution (Thermo Fisher Scientific) for 20 min and then washed with a warm medium. In specific experiments, cells were stained with 25 nM mitochondrion-selective probe MitoTracker® Red FM (Thermo Fisher Scientific) for 30 min and then washed with warm medium. Live-cell imaging experiments were performed on an epi-fluorescence microscope (Olympus IX-83, Olympus) equipped with a chamber incubator (Okolab, Pozzuoli, Italy) and light-emitting diode (LED) illumination (λ=590 nm for mCherry and MitoTracker; λ=660 nm for Vybrant™ DiD). During all imaging experiments, cells were kept at 37°C, 5% $CO_2$ and 95% humidity. Time-lapse images were taken with 500 ms of exposure time and one image was taken every 1 or 2 min. Images were acquired with a charge-coupled device (CCD) sensor at 12-bit depth (ORCA-D2, Hamamatsu) using a 20× air objective (Olympus, NA=0.75) or a 40× oil objective (Olympus, NA=1.3) with a spatial resolution of 1280×960 pixels.

### $Ca^{2+}$ imaging

In $Ca^{2+}$-imaging experiments, $2.0\times10^4$ cells were plated on a flat coverslip and cultured for 1–6 days, and subsequently were loaded with the membrane-permeable $Ca^{2+}$ dye Fluo-4 AM (Life Technologies) by incubation with 4 µM Fluo-4 AM (dissolved in anhydrous DMSO, 4 mM stock solution) and Pluronic F-127 20% solution in DMSO (Life Technologies) at a ratio of 1:1 in Ringer's solution (145 mM NaCl, 3 mM KCl, 1.5 mM $CaCl_2$, 1 mM $MgCl_2$, 10 mM glucose and 10 mM Hepes, pH 7.4) at 37°C for 30 min. After incubation, the cultures were washed with Ringer's solution for 20 min and then transferred to the stage of a Nikon Eclipse Ti-U inverted microscope equipped with a piezoelectric table (Nano-ZI Series 500 µm range, Mad City Labs), an HBO 103 W/2 mercury

short arc lamp (Osram, Munich, Germany), a mirror unit (465–495 nm excitation bandpass filter, 505 nm dichroic, 515–555 nm emission bandpass filter) and an Electron Multiplier CCD Camera C9100-13 (Hamamatsu Photonics, Japan). $Ca^{2+}$-imaging recordings were performed at room temperature and images were acquired using the NIS Element software (Nikon, Japan) with an S-Fluor 20×/0.75 NA objective, at a sampling rate of 3–10 Hz, with a spatial resolution of 256×256 pixels for 15 min. To avoid saturation of the signals, excitation light intensity was attenuated by ND4 and ND8 neutral density filters (Nikon, Tokyo, Japan).

For ratiometric $Ca^{2+}$-imaging experiments, cells were loaded with 1.5 µM Fluo-4 AM [dissolved in anhydrous DMSO (Sigma-Aldrich), 1.5 mM stock solution], 2.5 µM Fura Red AM [dissolved in anhydrous DMSO (Sigma-Aldrich), 2.5 mM stock solution] and 1 µl Pluronic F-127 20% solution in DMSO (Life Technologies) in 1 ml Ringer's solution for 30 min. After incubation, the cultures were washed with Ringer's solution for 20 min and then transferred to the stage of an epi-fluorescence microscope (Olympus IX-83, Olympus) equipped with a chamber incubator (Okolab, Pozzuoli, Italy), LED illumination (λ=490 nm for both Fluo-4 AM and Fura Red AM) and a CCD camera (ORCA-D2, Hamamatsu) with a dual sensor to record the fluorescence images from Fluo-4 AM (520±17.5 nm) and Fura Red AM (640±37.5 nm) simultaneously. During all imaging experiments, cells were kept at 37°C, 5% $CO_2$ and 95% humidity. Time-lapse images were taken with 300 ms of exposure time. All acquisitions were operated with a 20× air objective (Olympus, NA=0.75) or a 40× oil objective (Olympus, NA=1.3).

### Immunofluorescence

Cells were grown on coverslips for 2 days and subsequently washed with ice-cold PBS, then fixed with 4% paraformaldehyde for 10 min at room temperature, followed by permeabilization with PBS plus 0.1% Triton X-100, blocked with 3% BSA and incubated overnight with primary antibody anti-MCU mouse monoclonal (1:100; ab219827, Abcam, Cambridge, UK). The cells were then washed with PBS three times for 5 min each, and incubated with Alexa Fluor 488-labelled goat anti-mouse secondary antibody (1:400; Life Technologies) at room temperature for 1 h. The cells were examined with a confocal microscope (Nikon A1R).

### Western blotting

Cells were lysed in RIPA buffer (50 mM Tris-HCl, pH 7.4, 150 mM, NaCl, 5 mM EDTA, pH 8.0, 30 mM NaF, 1 mM $Na_3VO_4$, 40 mM β-glycerophosphate, 0.1 mM PMSF, protease inhibitors, 10% glycerol and 1% Nonidet-P40). Whole-cell extracts were fractionated by SDS-PAGE and transferred to a nitrocellulose membrane using a transfer apparatus according to the manufacturer's protocols (Bio-Rad). After incubation with 3% in TBST (10 mM Tris-HCl, pH 8.0, 150 mM NaCl, 0.5% Tween 20) for 1 h, the membrane was washed once with TBST and incubated with antibodies against MCU (1:500) at 4°C overnight and horseradish peroxidase (HRP)-conjugated actin (1:3000) at room temperature for 15 min. Membranes were washed three times for 10 min and incubated with a 1:3000 dilution of HRP-conjugated anti-mouse for 2 h. Blots were washed with TBST three times and developed with an ECL system (Amersham Biosciences) according to the manufacturer's protocols.

### Quantification of cell viability

The alamarBlue® (Thermo Fisher Scientific) assay was performed to evaluate the metabolic activity of U87 cells with and without MCU silencing, and HA cells with and without MCU overexpression. After transfection for 48 h, cells were washed in PBS pre-warmed at 37°C, after which 10% alamarBlue® in growth medium was added. After 4 h of incubation at 37°C, absorbance was measured at 570/600 nm wavelengths and percentage cell viability compared with the control group was calculated following the manufacturer's instructions.

Analysis of cell death was performed using the Annexin V-FITC Apoptosis Detection Kit (BioLegend) following the manufacturer's instructions. Briefly, cells, resuspended in Binding Buffer at a cell density of 2-5×$10^5$/ml were first stained with Annexin V-FITC (A-V) and, after washing, with PI (1 µg/ml). Cells were then analysed by FACSCanto III (BD Biosciences), using FACSDiva software. On the basis of PI and A-V staining, cells were considered live cells ($PI^-$/A-$V^-$), cells in early apoptosis ($PI^-$/A-$V^+$), cells in late apoptosis ($PI^+$/A-$V^+$) or necrotic cells ($PI^+$/A-$V^-$).

### Quantification and analysis of $Ca^{2+}$-imaging data

Acquired images were processed with the ImageJ software. The somas or sections of TMs were localized in a specific region of interest (ROI; see red outlined area in Fig. 1A), and a dark region in which no cells were visible was selected to compute the background, which was then subtracted from the whole image. $Ca^{2+}$ transients of each cell signal were extracted by setting a threshold equal to three times the s.d. of the baseline. The decay of $I_f(t)$ was fitted to a cubic spline $Y(t)$ interpolating $I_f(t)$ at 10 or 20 points. $Y(t)$ was then added to the original optical signal to compensate for dye bleaching, and the fractional optical signal was calculated as follows:

$$\frac{DF}{F_0} = \frac{Y(t) + I_f(t)}{I_f(0)}, \quad (1)$$

where $I_f(0)$ is the fluorescence intensity at the beginning of the recording.

For ratiometric $Ca^{2+}$ imaging, image sequences from Fluo-4 AM and Fura Red AM labelling were separated by ImageJ. A ROI for subtracting the background and ROIs around the cell bodies were then selected. Mean grey values from two channels were measured over time as shown in Fig. 1B and the amplitude of optical signals from the two dyes decayed because of bleaching. After background subtraction, $F1$ (cellular green emission by Fluo-4 AM) and $F2$ (cellular red emission by Fura Red AM) were used to calculate the fluorescence ratio R as follows:

$$R = F1/F2. \quad (2)$$

The time course of R was less affected by dye bleaching (Fig. 1C) because bleaching had almost the same time constant for Fluo-4 AM and Fura Red AM. When $F1$ increased and concomitantly $F2$ decreased, as in Fig. 1B, there is a genuine increase in $[Ca^{2+}]_i$. If $F1$ and $F2$ do not have changes with a similar time course with opposite polarity, fluorescent changes are usually caused by artefacts most commonly by the motion of visualized cells. GBM cells usually move significantly and in order to observe genuine changes of $[Ca^{2+}]_i$ it is necessary to use ratiometric $Ca^{2+}$ imaging

$[Ca^{2+}]_i$ measurements were performed as previously described (Assinger et al., 2015). Briefly, fluorescent cells were treated with ionomycin (5 µM) and R was measured with free $Ca^{2+}$ ranging from 0 to 28,000 nM by mixing Calcium Calibration Buffer 10 mM CaEGTA and Calcium Calibration Buffer zero (10 mM $K_2$EGTA) (Life Technologies) at different ratios. The following equation was used to determine $[Ca^{2+}]_i$ (Assinger et al., 2015):

$$[Ca^{2+}]_i = K_d \times (R - R_{min})/(R_{max} - R), \quad (3)$$

where $K_d$, $R_{min}$ and $R_{max}$ were obtained during $Ca^{2+}$ calibration experiments. In the calibration experiment illustrated in Fig. 1D, the obtained values of $K_d$, $R_{min}$ and $R_{max}$ were 810.3 nM, 0.56 and 4.60, respectively, which were obtained from averaging data of 32 GBM cells from three distinct experimental sessions.

### Statistical analysis

Data are shown as the mean±s.d. from at least three culture preparations. The quantified data were analysed with one-way analysis of variance (ANOVA) or two-way ANOVA, followed by Bonferroni post-hoc comparisons, using GraphPad Prism version 6.01. The number of replicas and statistical tests used for each experiment is specified in the figure legends or in the Results section. Significance was set to $*P<0.05$, $**P<0.01$ and $***P<0.001$.

#### Acknowledgements

We thank Prof. Antonello Mallamaci for his helpful suggestions on RNA interference experiments, and Diletta Pozzi, Nicola Galvanetto and Simone Mortal for help with data analysis and useful discussions.

#### Competing interests

The authors declare no competing or financial interests.

#### Author contributions

Conceptualization: M.S., Y.Y., V.T.; Methodology: X.L., R.S., A.B., D.C., F.C., I.M., V.T.; Formal analysis: X.L.; Data curation: X.L., R.S.; Writing - original draft: X.L.,

V.T.; Writing - review & editing: X.L., R.S., A.B., D.C., T.I., M.S., F.C., I.M., Y.Y., V.T.; Supervision: V.T.; Project administration: V.T.; Funding acquisition: D.C., V.T.

**Funding**
This work was supported by funds from Regione Autonoma Friuli Venezia Giulia for the projects 'Infiltrazione nei gliomi: nuovo target terapeutico – Glioblastoma' [No. 605/SPS] and 'ARES – Against brain cancer: finding personalized therapies with *in silico* and *in vitro* strategies' [No. 738/LAVFORU].

**Supplementary information**
Supplementary information available online at
http://jcs.biologists.org/lookup/doi/10.1242/jcs.237503.supplemental

**Peer review history**
The peer review history is available online at
https://jcs.biologists.org/lookup/doi/10.1242/jcs.236503.reviewer-comments.pdf

**References**

**Agarwal, A., Wu, P.-H., Hughes, E. G., Fukaya, M., Tischfield, M. A., Langseth, A. J., Wirtz, D. and Bergles, D. E.** (2017). Transient opening of the mitochondrial permeability transition pore induces microdomain calcium transients in astrocyte processes. *Neuron* **93**, 587-605.e7. doi:10.1016/j.neuron.2016.12.034

**Andolfi, L., Bourkoula, E., Migliorini, E., Palma, A., Pucer, A., Skrap, M., Scoles, G., Beltrami, A. P., Cesselli, D. and Lazzarino, M.** (2014). Investigation of adhesion and mechanical properties of human glioma cells by single cell force spectroscopy and atomic force microscopy. *PLoS ONE* **9**, e112582. doi:10.1371/journal.pone.0112582

**Arruda, A. P. and Hotamisligil, G. S.** (2015). Calcium homeostasis and organelle function in the pathogenesis of obesity and diabetes. *Cell Metab.* **22**, 381-397. doi:10.1016/j.cmet.2015.06.010

**Assinger, A., Volf, I. and Schmid, D.** (2015). A novel, rapid method to quantify intraplatelet calcium dynamics by ratiometric flow cytometry. *PLoS ONE* **10**, e0122527. doi:10.1371/journal.pone.0122527

**Basso, E., Rigotto, G., Zucchetti, A. E. and Pozzan, T.** (2018). Slow activation of fast mitochondrial $Ca^{2+}$ uptake by cytosolic $Ca^{2+}$. *J. Biol. Chem.* **293**, 17081-17094. doi:10.1074/jbc.RA118.002332

**Belmar, J. and Fesik, S. W.** (2015). Small molecule Mcl-1 inhibitors for the treatment of cancer. *Pharmacol. Ther.* **145**, 76-84. doi:10.1016/j.pharmthera.2014.08.003

**Bindocci, E., Savtchouk, I., Liaudet, N., Becker, D., Carriero, G. and Volterra, A.** (2017). Three-dimensional $Ca^{2+}$ imaging advances understanding of astrocyte biology. *Science* **356**, eaai8185. doi:10.1126/science.aai8185

**Bourkoula, E., Mangoni, D., Ius, T., Pucer, A., Isola, M., Musiello, D., Marzinotto, S., Toffoletto, B., Sorrentino, M., Palma, A. et al.** (2014). Glioma-associated stem cells: a novel class of tumor-supporting cells able to predict prognosis of human low-grade gliomas. *Stem Cells* **32**, 1239-1253. doi:10.1002/stem.1605

**Caro, A. A. and Cederbaum, A. I.** (2002). Role of calcium and calcium-activated proteases in CYP2E1-dependent toxicity in HEPG2 cells. *J. Biol. Chem.* **277**, 104-113. doi:10.1074/jbc.M107864200

**Curry, M. C., Peters, A. A., Kenny, P. A., Roberts-Thomson, S. J. and Monteith, G. R.** (2013). Mitochondrial calcium uniporter silencing potentiates caspase-independent cell death in MDA-MB-231 breast cancer cells. *Biochem. Biophys. Res. Commun.* **434**, 695-700. doi:10.1016/j.bbrc.2013.04.015

**Dong, Z., Shanmughapriya, S., Tomar, D., Siddiqui, N., Lynch, S., Nemani, N., Breves, S. L., Zhang, X., Tripathi, A., Palaniappan, P. et al.** (2017). Mitochondrial Ca(2+) uniporter is a mitochondrial luminal redox sensor that augments MCU channel activity. *Mol. Cell* **65**, 1014-1028 e1017. doi:10.1016/j.molcel.2017.01.032

**Drago, I., De Stefani, D., Rizzuto, R. and Pozzan, T.** (2012). Mitochondrial Ca2+ uptake contributes to buffering cytoplasmic Ca2+ peaks in cardiomyocytes. *Proc. Natl. Acad. Sci. USA* **109**, 12986-12991. doi:10.1073/pnas.1210718109

**Farfariello, V., Iamshanova, O., Germain, E., Fliniaux, I. and Prevarskaya, N.** (2015). Calcium homeostasis in cancer: a focus on senescence. *Biochim. Biophys. Acta* **1853**, 1974-1979. doi:10.1016/j.bbamcr.2015.03.005

**Fischer, T. H., Herting, J., Tirilomis, T., Renner, A., Neef, S., Toischer, K., Ellenberger, D., Forster, A., Schmitto, J. D., Gummert, J. et al.** (2013). $Ca^{2+}$/calmodulin-dependent protein kinase II and protein kinase A differentially regulate sarcoplasmic reticulum $Ca^{2+}$ leak in human cardiac pathology. *Circulation* **128**, 970-981. doi:10.1161/CIRCULATIONAHA.113.001746

**Foskett, J. K. and Philipson, B.** (2015). The mitochondrial $Ca^{2+}$ uniporter complex. *J. Mol. Cell. Cardiol.* **78**, 3-8. doi:10.1016/j.yjmcc.2014.11.015

**Hall, D. D., Wu, Y., Domann, F. E., Spitz, D. R. and Anderson, M. E.** (2014). Mitochondrial calcium uniporter activity is dispensable for MDA-MB-231 breast carcinoma cell survival. *PLoS ONE* **9**, e96866. doi:10.1371/journal.pone.0096866

**Hamilton, J., Brustovetsky, T., Rysted, J. E., Lin, Z., Usachev, Y. M. and Brustovetsky, N.** (2018). Deletion of mitochondrial calcium uniporter incompletely inhibits calcium uptake and induction of the permeability transition pore in brain mitochondria. *J. Biol. Chem.* **293**, 15652-15663. doi:10.1074/jbc.RA118.002926

**Harley, W., Floyd, C., Dunn, T., Zhang, X. D., Chen, T. Y., Hegde, M., Palandoken, H., Nantz, M. H., Leon, L., Carraway, K. L.Jr** et al. (2010). Dual inhibition of sodium-mediated proton and calcium efflux triggers non-apoptotic cell death in malignant gliomas. *Brain Res.* **1363**, 159-169. doi:10.1016/j.brainres.2010.09.059

**Jackson, J. G. and Robinson, M. B.** (2015). Reciprocal regulation of mitochondrial dynamics and calcium signaling in astrocyte processes. *J. Neurosci.* **35**, 15199-15213. doi:10.1523/jneurosci.2049-15.2015

**Koch, K. W. and Dell'orco, D.** (2013). A calcium-relay mechanism in vertebrate phototransduction. *ACS Chem. Neurosci.* **4**, 909-917. doi:10.1021/cn400027z

**Krizaj, D. and Copenhagen, D. R.** (2002). Calcium regulation in photoreceptors. *Front. Biosci.* **7**, d2023-d2044. doi:10.2741/A896

**Leclerc, C., Haeich, J., Aulestia, F. J., Kilhoffer, M. C., Miller, A. L., Neant, I., Webb, S. E., Schaeffer, E., Junier, M. P., Chneiweiss, H. et al.** (2016). Calcium signaling orchestrates glioblastoma development: facts and conjunctures. *Biochim. Biophys. Acta* **1863**, 1447-1459. doi:10.1016/j.bbamcr.2016.01.018

**Liu, K. H., Yang, S. T., Lin, Y. K., Lin, J. W., Lee, Y. H., Wang, J. Y., Hu, C. J., Lin, E. Y., Chen, S. M., Then, C. K. et al.** (2015). Fluoxetine, an antidepressant, suppresses glioblastoma by evoking AMPAR-mediated calcium-dependent apoptosis. *Oncotarget* **6**, 5088-5101. doi:10.18632/oncotarget.3243

**Mammucari, C., Gherardi, G. and Rizzuto, R.** (2017). Structure, activity regulation, and role of the mitochondrial calcium uniporter in health and disease. *Front. Oncol.* **7**, 139. doi:10.3389/fonc.2017.00139

**Marchi, S. and Pinton, P.** (2016). Alterations of calcium homeostasis in cancer cells. *Curr. Opin. Pharmacol.* **29**, 1-6. doi:10.1016/j.coph.2016.03.002

**McFerrin, M. B., Turner, K. L., Cuddapah, V. A. and Sontheimer, H.** (2012). Differential role of IK and BK potassium channels as mediators of intrinsic and extrinsic apoptotic cell death. *Am. J. Physiol. Cell Physiol.* **303**, C1070-C1078. doi:10.1152/ajpcell.00040.2012

**Osswald, M., Jung, E., Sahm, F., Solecki, G., Venkataramani, V., Blaes, J., Weil, S., Horstmann, H., Wiestler, B., Syed, M. et al.** (2015). Brain tumour cells interconnect to a functional and resistant network. *Nature* **528**, 93-98. doi:10.1038/nature16071

**Osuka, S. and Van Meir, E. G.** (2017). Overcoming therapeutic resistance in glioblastoma: the way forward. *J. Clin. Investig.* **127**, 415-426. doi:10.1172/JCI89587

**Pollard, S. M., Yoshikawa, K., Clarke, I. D., Danovi, D., Stricker, S., Russell, R., Bayani, J., Head, R., Lee, M., Bernstein, M. et al.** (2009). Glioma stem cell lines expanded in adherent culture have tumor-specific phenotypes and are suitable for chemical and genetic screens. *Cell Stem Cell* **4**, 568-580. doi:10.1016/j.stem.2009.03.014

**Rand, V., Prebble, E., Ridley, L., Howard, M., Wei, W., Brundler, M. A., Fee, B. E., Riggins, G. J., Coyle, B., Grundy, R. G. et al.** (2008). Investigation of chromosome 1q reveals differential expression of members of the S100 family in clinical subgroups of intracranial paediatric ependymoma. *Br. J. Cancer* **99**, 1136-1143. doi:10.1038/sj.bjc.6604651

**Ren, T., Wang, J., Zhang, H., Yuan, P., Zhu, J., Wu, Y., Huang, Q., Guo, X., Zhang, J., Ji, L. et al.** (2018). MCUR1-mediated mitochondrial calcium signaling facilitates cell survival of hepatocellular carcinoma via reactive oxygen species-dependent P53 degradation. *Antioxid Redox Signal.* **28**, 1120-1136. doi:10.1089/ars.2017.6990

**Robil, N., Petel, F., Kilhoffer, M. C. and Haiech, J.** (2015). Glioblastoma and calcium signaling - analysis of calcium toolbox expression. *Int. J. Dev. Biol.* **59**, 407-415. doi:10.1387/ijdb.150200jh

**Schwaller, B.** (2010). Cytosolic Ca2+ buffers. *Cold Spring Harb. Perspect. Biol.* **2**, a004051. doi:10.1101/cshperspect.a004051

**Shanmughapriya, S., Rajan, S., Hoffman, N. E., Zhang, X., Guo, S., Kolesar, J. E., Hines, K. J., Ragheb, J., Jog, N. R., Caricchio, R. et al.** (2015). $Ca^{2+}$ signals regulate mitochondrial metabolism by stimulating CREB-mediated expression of the mitochondrial $Ca^{2+}$ uniporter gene MCU. *Sci. Signal.* **8**, ra23. doi:10.1126/scisignal.2005673

**Shin, D. H., Leem, D. G., Shin, J. S., Kim, J. I., Kim, K. T., Choi, S. Y., Lee, M. H., Choi, J. H. and Lee, K. T.** (2018). Compound K induced apoptosis via endoplasmic reticulum $Ca^{2+}$ release through ryanodine receptor in human lung cancer cells. *J. Ginseng Res.* **42**, 165-174. doi:10.1016/j.jgr.2017.01.015

**Steven, A. and Seliger, B.** (2016). Control of CREB expression in tumors: from molecular mechanisms and signal transduction pathways to therapeutic target. *Oncotarget* **7**, 35454-35465. doi:10.18632/oncotarget.7721

**Teich, A. F., Nicholls, R. E., Puzzo, D., Fiorito, J., Purgatorio, R., Fa', M. and Arancio, O.** (2015). Synaptic therapy in Alzheimer's disease: a CREB-centric approach. *Neurotherapeutics* **12**, 29-41. doi:10.1007/s13311-014-0327-5

**Tombal, B., Denmeade, S. R., Gillis, J. M. and Isaacs, J. T.** (2002). A supramicromolar elevation of intracellular free calcium ($[Ca^{2+}]_i$) is consistently required to induce the execution phase of apoptosis. *Cell Death Differ.* **9**, 561-573. doi:10.1038/sj.cdd.4400999

**Tosatto, A., Sommaggio, R., Kummerow, C., Bentham, R. B., Blacker, T. S., Berecz, T., Duchen, M. R., Rosato, A., Bogeski, I., Szabadkai, G. et al.** (2016).

The mitochondrial calcium uniporter regulates breast cancer progression via HIF-1alpha. *EMBO Mol. Med.* **8**, 569-585. doi:10.15252/emmm.201606255

**Villalobos, C., Sobradillo, D., Hernández-Morales, M. and Núñez, L.** (2017). Calcium remodeling in colorectal cancer. *Biochim. Biophys. Acta Mol. Cell Res.* **1864**, 843-849. doi:10.1016/j.bbamcr.2017.01.005

**Vultur, A., Gibhardt, C. S., Stanisz, H. and Bogeski, I.** (2018). The role of the mitochondrial calcium uniporter (MCU) complex in cancer. *Pflugers Arch.* **470**, 1149-1163. doi:10.1007/s00424-018-2162-8

**Zhivotovsky, B. and Orrenius, S.** (2011). Calcium and cell death mechanisms: a perspective from the cell death community. *Cell Calcium* **50**, 211-221. doi:10.1016/j.ceca.2011.03.003

**Ziegler, D. S., Wright, R. D., Kesari, S., Lemieux, M. E., Tran, M. A., Jain, M., Zawel, L. and Kung, A. L**. (2008). Resistance of human glioblastoma multiforme cells to growth factor inhibitors is overcome by blockade of inhibitor of apoptosis proteins. *J. Clin. Investig.* **118**, 3109-3122. doi:10.1172/JCI34120